

# A Diffeomorphic Vector Field Approach to Analyze the Thickness of the Hippocampus from 7T MRI

Alexis Guyot \*, Ana B. Graciano Fouquier \*, Émilie Gerardin \*, Marie Chupin, Joan A. Glaunès, Linda Marrakchi-Kacem, Johanne Germain, Claire Boutet, Claire Cury, Lucie Hertz-Pannier, Alexandre Vignaud, Stanley Durrleman, Thomas R. Henry, Pierre-François van de Moortele, Alain Trouvé and Olivier Colliot

**Abstract**—**OBJECTIVE.** 7-Tesla MRI of the hippocampus enhances the visualization of its internal substructures. Among these substructures, the cornu Ammonis and subiculum form a contiguous folded ribbon of gray matter. Here, we propose a method to analyze local thickness measurements of this ribbon. **METHODS.** We introduce an original approach based upon the estimation of a diffeomorphic vector field that traverses the ribbon. The method is designed to handle specificities of the hippocampus and corresponding 7-Tesla acquisitions: highly convoluted surface, non-closed ribbon, incompletely defined inner/outer boundaries, anisotropic acquisitions. We furthermore propose to conduct group comparisons using a population template built from the central surfaces of individual subjects. **RESULTS.** We first assessed the robustness of our approach to anisotropy, as well as to inter-rater variability, on a post-mortem scan and on *in vivo* acquisitions respectively. We then conducted a group study on a dataset of *in vivo* MRI from temporal lobe epilepsy (TLE) patients and healthy controls. The method detected local thinning patterns in patients, predominantly ipsilaterally to the seizure focus, which is consistent with medical knowledge. **CONCLUSION.** This new technique allows measuring the thickness of the hippocampus from 7-Tesla MRI. It shows good robustness with respect to anisotropy and inter-rater variability and has the potential to detect local atrophy in patients. **SIGNIFICANCE.** As 7-Tesla MRI is increasingly available, this new method may become a useful tool to study local alterations of the hippocampus in brain disorders. It is made freely available to the community (code: <https://github.com/aramis-lab/hiplay7-thickness>, post-mortem segmentation: <https://doi.org/10.5281/zenodo.3533264>).

**Index Terms**—Morphometry, Thickness, Diffeomorphism, Magnetic Resonance Imaging, Hippocampus, Ultra-high-field, 7-Tesla.

This work was supported by ANR (HM-TC, ANR-09-EMER-006), France Alzheimer (IRMA7), by the CATI project, by Investissements d’avenir ANR-19-P3IA-0001 (PRAIRIE 3IA Institute) and ANR-10-IAIHU-06, by the Philippe foundation, and by the NSF/NIH/ANR program “Collaborative Research in Computational Neuroscience” (HIPLAY7, NSF-CRCSN-1607835 and ANR-16-NEUC-0001-01).

\* Denotes equal first authors

A. Guyot, S. Durrleman, O. Colliot (olivier.colliot@upmc.fr) are with 1, 2 ; A. B. Graciano Fouquier, É. Gerardin, L. Marrakchi-Kacem, J. Germain, C. Boutet, C. Cury, were with 1, 2 ; M. Chupin is with 1, 3 ; J. A. Glaunès is with 4 ; L. Hertz-Pannier is with 5, 6 ; A. Vignaud is with 5 ; T. R. Henry is with 7 ; P.-F. van de Moortele is with 8 ; A. Trouvé is with 9. Where 1. ICM, Inserm, U 1127, CNRS, UMR 7225, Sorbonne Université, Paris, France ; 2. Inria, Paris, France ; 3. CATI, Paris, France ; 4. MAP5, Université Paris Descartes, France ; 5. NeuroSpin, I2BM, DSV, CEA, Gif-sur-Yvette, France ; 6. UMR 1129, INSERM; CEA; Université Paris Descartes, Paris, France ; 7. Department of Neurology, University of Minnesota, Minneapolis, MN, USA ; 8. Center for Magnetic Resonance Research, University of Minnesota, Minneapolis, MN, USA ; 9. CMLA, CNRS UMR 8536, Cachan, France.

## I. INTRODUCTION

THE hippocampus is a structure of the medial temporal lobe of the brain which plays a crucial role in various neurological and psychiatric diseases including epilepsy, Alzheimer’s disease, schizophrenia and depression [1]. The hippocampus is a highly complex arrangement of histologically and functionally distinct regions [2]. In particular, the gray matter part of the hippocampus is mainly composed of a larger ribbon, called Ammon’s horn or cornu Ammonis (CA), folded around a small gyrus, called the dentate gyrus (DG). The cornu Ammonis is further composed of four sectors: CA1-4. CA1 is the largest sector and is continuous with the subiculum. Moreover, subregions are composed of different layers that vary in terms of cellular composition. The stratum pyramidale (SP) is richer in neuronal bodies whereas the strata radiatum, lacunosum and moleculare (SRLM) are poorer in neuronal bodies. Histological studies have shown that hippocampal subregions present differential vulnerability to distinct diseases, such as temporal lobe epilepsy (TLE) [3] and Alzheimer’s disease [4].

However, the internal organization of the hippocampus is not precisely identifiable in conventional anatomical MRI [5]. Thus, various new acquisition and segmentation protocols, usually based on T2-weighted or proton-density MRI with submillimetric coronal in-plane resolution, have been proposed in order to visualize and delineate hippocampal subregions *in vivo* (see [5] for a review). Initial studies (e.g., [6]) were made using 3T or 4.7T MRI. Ultra-high field MRI ( $\geq 7T$ ) provides enhanced contrasts, increased signal-to-noise ratio, higher coronal in-plane resolution (approx. 0.2-0.3mm) and thinner slices (approx. 1mm) [7], [8], [9], enabling more accurate and consistent 3D reconstructions of the internal structures.

These advanced imaging approaches have been applied to perform volumetry of hippocampal subregions in different diseases, inclusive of TLE [10], [11] and Alzheimer’s disease [12], [13]. Nevertheless, volumetric studies potentially fail to identify highly localised changes within the hippocampal subregions. In the case of the cerebral cortex, local atrophy is often analyzed through local thickness measurements mapped onto a surface representation of the cortical ribbon [14]. Extensive literature documents thickness estimation for the cortex (see [15] for a 2011 review). In the same spirit, for the hippocampus, local thickness measures would be well adapted to the gray matter ribbon of the hippocampus.

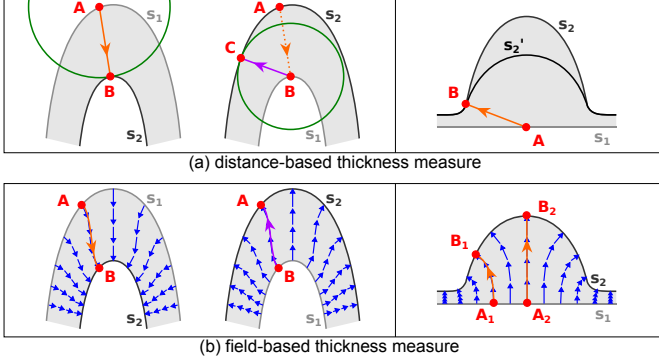


Fig. 1: Thickness measures from surface  $s_1$  to surface  $s_2$ . **(a)** Left: the thickness at  $A$  is defined as the distance to its closest point  $B$  on  $s_2$ . With  $s_1$  and  $s_2$  interchanged,  $B$  is mapped to  $C$ , which differs from  $A$ , rendering the measure asymmetrical. Right: erroneously, the method returns the same thickness at  $A$  for both the “large” ( $s_2$ ) and the “small” ( $s'_2$ ) hump. **(b)** Left: a vector field spans the domain within  $s_1$  and  $s_2$  and each point  $A$  on  $s_1$  is linked to a unique point  $B$  on  $s_2$  via a streamline. Swapping  $s_1$  and  $s_2$  changes the orientation of the vector field but has no effect on the position of streamlines, making the approach symmetrical. Right: the computation of thickness for the “field-based” method is not confounded by the hump shape.

In the following, we refer to this ribbon as *hippocampal ribbon*, corresponding to the contiguous union of both CA-SP and subiculum-SP. However, methods designed for cortical thickness analysis are not directly applicable to the hippocampus because of its specificities: the ribbon is not closed, its inner/outer boundaries are usually incompletely defined in segmentation protocols, corresponding image acquisitions are often highly anisotropic (with higher coronal in-plane resolution). Several papers have proposed to measure hippocampal thickness using a manual (with some possible semi-automated steps) on 2D slices (e.g. [16], [17]) with interesting applications to different diseases (including Alzheimer’s and Parkinson’s diseases). However, manual measurement is time-consuming and working in 2D may lead to biased thickness estimates. Image processing tools to measure the thickness of the hippocampal ribbon are still in their infancy, and, to the best of our knowledge, only three families of such methods (corresponding to five publications [18], [19], [20], [21], [22]) have been put forward to the community. The first relies on an unfolding technique initially proposed in [23] to study functional activation maps in hippocampal subregions and later used in several works [18], [19], [20] to compute thickness across these subregions. The method in [18] can successfully unveil local atrophy, yet has some methodological limitations. First, working with unfolded maps discards the information concerning the convolution of the ribbon, which may be of interest to study the variability of the folding pattern. Also, the thickness maps produced in the 3D space are based on Euclidean distances to the boundaries of the ribbon. However, Euclidean metrics are not necessarily well adapted to convoluted surfaces (see Fig. 1a). Such metrics are indeed asymmetric, where interchanging starting and ending surfaces results in different point correspondences between those two (Fig. 1a, left). In addition, using an Euclidean

distance can lead to a dramatic underestimation of thickness in case of pronounced humps (Fig. 1a, right). Second, in an article mainly devoted to segmentation of the hippocampal subfields, [21] presented a method to skeletonize the subregions and compute thickness maps over the surface of the hippocampal gray matter. Thickness measures were defined at any point of the surface as the Euclidean distance to the closest point on the skeleton, with thickness values left undefined anywhere else within the volume. As illustrated in Fig. 1, thickness measures based on Euclidean distances are ill-behaved. Also, the skeleton extraction in [21] strongly depends on a pruning step that must be carefully configured to remove spurious branches. Last, [22] unfolded the gray matter of the hippocampus and mapped 3D thickness along its laminar dimension by applying the Laplace equation as described in [24]. Thickness values were computed as the length of each individual streamlines spanning the output vector field (see Fig. 1b), resulting in a symmetric formulation of thickness (Fig. 1b, left) that is better suited (Fig. 1b, right) to convoluted shapes than “Euclidean distance-based” definitions. However, this approach has not been designed with the fact that MR acquisitions can be highly anisotropic, which is a concern as such data is frequently acquired to visualize the hippocampal subfields.

In this paper, we propose a method to simultaneously estimate a local thickness map and extract a central surface representation over the entire length of the hippocampus, from a segmentation of the *hippocampal ribbon* on ultra-high resolution 7T MRI data. Our method matches points on inner and outer boundaries with a symmetric, non-ambiguous mapping consisting of trajectories smooth enough to cope with high-curvature regions. The core of the approach consists of a new variational method to estimate a diffeomorphic (invertible and smooth) vector field that traverses the ribbon from inner to outer boundary, the smoothness of which is controlled through its norm in a Reproducing Kernel Hilbert Space (RKHS) [25]. From the vector field, point-to-point correspondences are computed between the inner and outer boundaries along curved streamlines, the lengths of which are used to deduce thickness values as well as a central surface representation. This novel approach allows dealing with the specificities of 7T MR imaging of the hippocampus, enabling it to handle incompletely defined inner/outer boundaries, helping it deal better with the strong anisotropy present in most acquisition protocols and letting it cope with highly convoluted hippocampal regions.

The approach was evaluated using three types of experiments. First, we evaluated its robustness to anisotropy by simulating anisotropic acquisitions from a quasi-isotropic segmentation of a postmortem specimen acquired and described in [10]. Then, we assessed the impact of inter-rater variability on thickness measurements using a set of four *in vivo* 7T MR images of control subjects segmented by two different raters. Last, we studied the ability of the method to detect local alterations associated to pathologies, using a set of 8 patients with TLE epilepsy and of 9 healthy controls.

The rest of this paper is organized as follows. Section II presents the estimation of the central surface and thickness

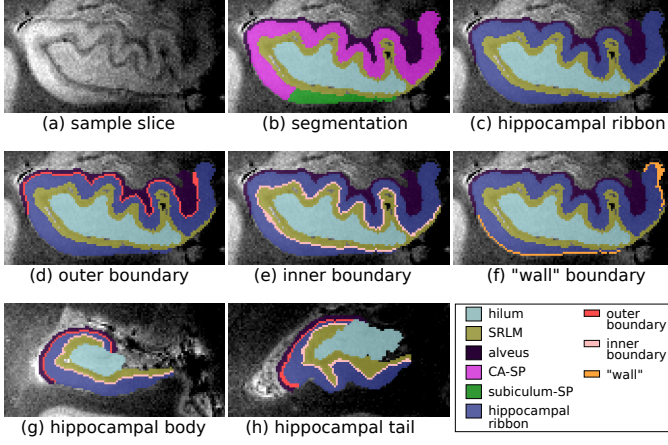


Fig. 2: Manual segmentation of hippocampal subregions and extraction of boundaries **(a)** Sample slice of the hippocampal head. **(b)** Segmented subregions: CA-SP (magenta), subiculum-SP (green), alveus (dark purple), SRLM (yellow), and hilum (cyan). **(c)** Hippocampal ribbon (blue): merge CA-SP and subiculum-SP. **(d)** Outer boundary (red): points adjacent to the alveus. **(e)** Inner boundary (pink): points adjacent to the SRLM. **(f)** “Wall” (orange): remaining uncertain boundary points are labeled as inner/outer simultaneously to the thickness map estimation. The two last panels display the same regions as **(d)** and **(e)** in the hippocampal body **(g)** and tail **(h)**.

map. Experiments and results are described in Section III. Finally, an overall discussion is given in Section IV.

## II. CENTRAL SURFACE AND THICKNESS ESTIMATION

Our approach takes as input a segmentation (see Fig. 2a and b, illustrated on the post-mortem data from [10]) across the hippocampal head, body and tail of the following subregions: 1) alveus; 2) SRLM corresponding to the strata radiatum, lacunosum and moleculare of CA1-3 and the strata lacunosum and moleculare of the subiculum (the layers poorer in neuronal bodies); 3) hilum corresponding to the stratum pyramidale of CA4 and the stratum granulosum and polymorphic layer of DG, which are the layers richer in neuronal bodies; 4) Cornu Ammonis Stratum Pyramidale (CA-SP), assumed to correspond to the stratum pyramidale of CA1-3, the layer richer in neuronal bodies of CA1-3; 5) subiculum-SP corresponding to the stratum pyramidale of the subiculum, layer richer in neuronal bodies of the subiculum. Throughout this article, the above structures are manually delineated across the full length of the hippocampus, following an extension of the protocol of [11]. The extension is described in Appendix I.

Following the segmentation described above, the hippocampal ribbon is obtained by merging CA-SP and subiculum-SP (Fig. 2c). Next, we extract the ribbon inner and outer borders according to their vicinity to other segmented regions: voxels neighboring the alveus are assigned to the ribbon outer boundary (Fig. 2d), whereas voxels next to the SRLM are assigned to the inner boundary (Fig. 2e). Initially, some boundary points belong neither to the inner nor to the outer boundary (“wall” boundary points, Fig. 2f). They will be assigned automatically by the method. The same procedure is repeated on the body (Fig. 2g) and tail (Fig. 2h) of the hippocampus. Contingent on these boundaries, our overall thickness method (illustrated

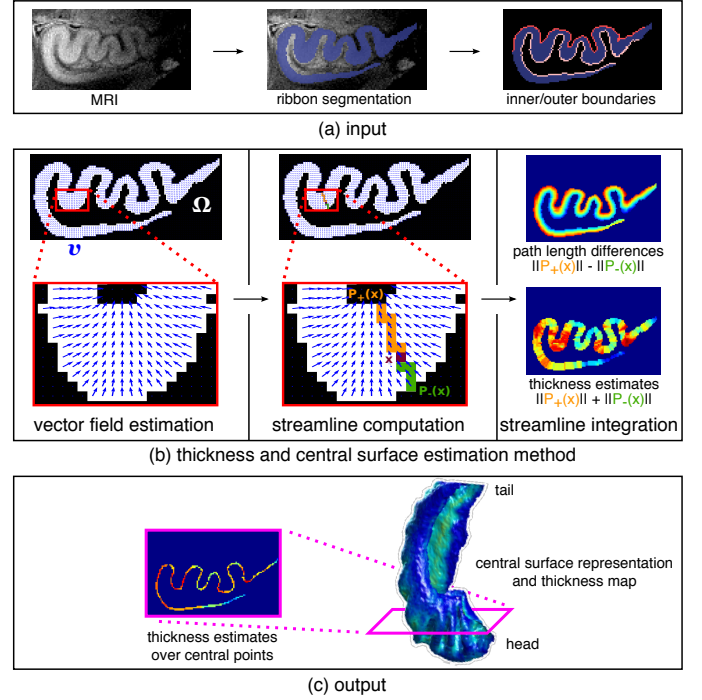


Fig. 3: **(a)** The inner and outer boundaries are automatically extracted from a segmentation of the hippocampal ribbon in a T2-weighted MRI. **(b)** Left: A vector field  $v$  is estimated from the inner to the outer boundary of the ribbon domain  $\Omega$ . Center: For each point  $x$  within  $\Omega$ , the streamlines  $P_+(x)$  and  $P_-(x)$  connecting  $x$  to outer/inner boundary respectively are generated from the vector field, solving a differential equation. Right: Path length differences are computed at all  $x$  as the difference between  $\|P_+(x)\|$  and  $\|P_-(x)\|$ , while thickness values are estimated as their sum. **(c)** The central surface representation is defined as the set of points with a path length difference of 0. For all these points, thickness estimates are collected, yielding a compact 3D representation of the hippocampal ribbon with its associated thickness map.

in Fig. 3) estimates a diffeomorphic vector field through the ribbon, derives streamlines along the field and from the lengths of those deduce local thickness values.

### A. A variational approach for vector field estimation

Let  $\Omega \subset \mathbb{R}^d$  ( $d = 2$  or  $d = 3$ ) be the hippocampal ribbon,  $\partial\Omega$  its boundary, and  $n$  the outward normal to  $\partial\Omega$ . We further break  $\partial\Omega$  into its inner ( $\partial\Omega_i$ ), outer ( $\partial\Omega_o$ ) and “wall” ( $\partial\Omega_w$ ) parts, such that  $\partial\Omega = \partial\Omega_i \cup \partial\Omega_o \cup \partial\Omega_w$ . We shall build a smooth vector field  $v$  running from  $\partial\Omega_i$  to  $\partial\Omega_o$  based on a set of physically-motivated and intuitive assumptions (inspired by criteria from [24]): 1) it must produce unique trajectories that do not cross each other, in order to guarantee a unique thickness value for each point; 2) it must go through  $\Omega$  by following the most direct trajectory from the inner to the outer boundary, which should correspond to computing the thinnest thickness values; 3) it must be smooth enough to cope with the high-curvature regions; 4) no trajectory should stop inside the volume, to ensure that any point on one boundary has a corresponding point on the opposite boundary. From  $v$ , we shall evaluate the thickness at any point of  $\partial\Omega$  by mapping it to its counterpart on the opposite boundary via a

trajectory (*streamline*) derived from the field and by measuring the distance along the streamline.

The transverse vector field above is defined as the solution of the variational formulation presented below. Consider  $x \in \partial\Omega$  and let  $\epsilon : \partial\Omega \rightarrow \{-1; 0; 1\}$  be a function defining the orientation of the normal vector in  $\partial\Omega$  such that:

$$\epsilon(x) = \begin{cases} -1 & , \text{ if } x \in \partial\Omega_i \quad (\text{inward orientation}) \\ 0 & , \text{ if } x \in \partial\Omega_w \\ 1 & , \text{ if } x \in \partial\Omega_o \quad (\text{outward orientation}) \end{cases}$$

A vector space  $V$  is characterized by the choice of a kernel  $K : \mathbb{R}^d \times \mathbb{R}^d \rightarrow \mathbb{R}$ , such that, for any  $(v, x, \alpha) \in V \times \mathbb{R}^d \times \mathbb{R}^d$ :

$$\langle v(x), \alpha \rangle_{\mathbb{R}^d} = \langle v, K(\cdot, x) \alpha \rangle_V. \quad (1)$$

We estimate  $v$  by maximizing the following functional:

$$J(u, v) = \int_{\partial\Omega} \langle v, \epsilon n \rangle d\sigma + \int_{\Omega} \langle v, u \rangle dx - \frac{1}{2} \|v\|_V^2 \quad (2)$$

where  $u$  is a unit vector field on  $\Omega$  and  $\|\cdot\|_V$  is the Hilbert norm of  $v \in V$ , which is an RKHS. We refer the reader to Appendix II for the main definitions and theorems of the underlying vector spaces and RKHS theory adopted throughout this section.

The first term is the unsigned flux of the vector field. It drives the field in a direction close to the surface normal. The second term enforces vectors in  $\Omega$  to have nonzero norm, in order to construct continuous streamlines inside the volume. The last term controls the regularity of the vector field. By controlling its norm, we ensure that it will be smooth enough and not suffer from small irregularities at the boundaries. Note that using a regularizing kernel provides diffeomorphic flows.

As mentioned above, at the initialization, some boundary points belong neither to the inner nor to the outer boundary (Fig. 2f). For these points, the value of  $\epsilon$  will be estimated automatically. We thus optimize  $J(u, v, \epsilon)$  rather than  $J(u, v)$ .

### B. Functional maximization

Optimization of  $u$ , for  $v$  fixed, is straightforward:  $u = \frac{v}{\|v\|}$ . Optimization of  $\epsilon$  is performed only in the unknown regions where  $\epsilon$  was not explicitly marked, i.e.,  $\epsilon = \text{sgn}(\langle v, n \rangle)$ . Elsewhere, the values of  $\epsilon$  are fixed. If both  $u$  and  $\epsilon$  are fixed, the problem is quadratic:

$$\begin{aligned} J(u, v) &= \frac{1}{2} \int_{\Omega} u(y)^T K(x, y) u(x) dx dy \\ &+ \int_{\partial\Omega} \epsilon(y)^T n(y) K(x, y) \epsilon(x) n(x) d\sigma(x) d\sigma(y) \quad (3) \\ &= \frac{1}{2} \|u + \epsilon n\|_V^* \end{aligned}$$

The vector field  $v$  can be easily calculated from the formula:

$$v(x) = \int_{\partial\Omega} K(x, y) \epsilon(y) n(y) d\sigma(y) + \int_{\Omega} K(x, y) u(y) dy \quad (4)$$

See Appendix III for a proof of this result.

### C. Central surface computation and thickness estimation

Given a vector field  $v : \Omega \rightarrow \mathbb{R}^d$  (Fig. 3b, left) and a point  $x_0 \in \Omega$ , one can compute the trajectory (*streamline*)

followed by  $x_0$  according to the integration of  $v$ . As they are defined by a diffeomorphic flow, two distinct streamlines never cross each other, and for any point  $x_0$  on  $\Omega$ , there is a unique streamline connecting a point on one boundary to a point on the opposite one and passing through  $x_0$  by following  $v$ . For each  $x \in \Omega$ , consider two different streamlines starting from  $x$ :  $P_+(x)$ , which follows the field  $v$  towards the outer boundary, and  $P_-(x)$ , which follows the field  $-v$  and reaches the inner boundary (Fig. 3b, center). We then define the *thickness* at point  $x$  as the sum of  $D_+(x) = \text{length}(P_+(x))$  and  $D_-(x) = \text{length}(P_-(x))$  (Fig. 3b, right). Therefore, by definition, the thickness along a streamline is constant. Finally, the *central surface* of  $\Omega$  is defined as the zero level set of the function  $D_+ - D_-$  (Fig. 3c).

### D. Extension to anisotropic images

With a few exceptions, e.g., [7], [8], [22], acquisitions dedicated to the visualization of hippocampal subregions are highly anisotropic with respect to the anterior-posterior direction. We introduce an anisotropy term in the functional to address this issue directly from the raw (uninterpolated) data. Let  $\Phi$  be an application that maps a volume  $\Omega$  in physical space to a volume  $\tilde{\Omega} = \Phi(\Omega)$  in the image space. In our case,  $\Phi$  is a linear transformation of type  $\Phi(x, y, z) = (x, y, z/a)$  where  $a$  is the anisotropy factor. We define  $\Psi = \Phi^{-1}$ , and we denote by  $A$  the matrix of the application  $D\Phi$ , and by  $\tilde{n}$  the normal at  $\partial\tilde{\Omega}$ . Also, let  $K_p$  be the kernel in physical space and  $K_i$  the kernel in image space, such that  $K_i(x, y) = K_p(\Phi(x), \Phi(y))$ , and  $V_p$  and  $V_i$ , be, respectively, the RKHS of  $K_p$  and  $K_i$ .

The vector field  $\tilde{v}$  in the image space is given by:

$$\begin{aligned} \tilde{v}(x) &= \int_{\tilde{\Omega}} K_i(x, y) \frac{u(y)}{\det(A)} dy \\ &+ \int_{\partial\tilde{\Omega}} K_i(x, y) \tilde{\epsilon}(y) \frac{A^T \tilde{n}(y)}{\det(A)} d\tilde{\sigma}(y) \end{aligned} \quad (5)$$

See Appendix III for a proof of this result.

### E. Computational implementation of the RKHS Kernel

Proper discretization is needed to apply the proposed framework to the construction of central surfaces from imaging data. We shall assume that the volume  $\Omega \subset \mathbb{R}^d$  corresponding to the hippocampal ribbon is discretized over a  $d$ -dimensional grid, which defines a set of  $n$  voxels denoted by  $I$ , and the boundary voxels of which are denoted by  $B \subset I$ . Let  $x_i$  and  $x_j$  represent two points on the grid. We denote the kernel function applied to two grid points by  $K_{i,j} = K(u_i, u_j)$ , where  $u_i = u(x_i)$  denotes the vector representation of  $x_i$ , with a similar notation adopted for  $u_j$ . The discretized formulation of the square of the dual norm in (3) is then given by:

$$\begin{aligned} J(u_i, u_j) &= \frac{1}{2} \left( \sum_{x_i \in I} \sum_{x_j \in I} K_{i,j} \langle u_i, u_j \rangle + \sum_{x_i \in B} \sum_{x_j \in B} K_{i,j} \langle \epsilon_i n_i, \epsilon_j n_j \rangle \right. \\ &\quad \left. + 2 \sum_{x_i \in I} \sum_{x_j \in B} K_{i,j} \langle u_i, \epsilon_j n_j \rangle \right) \end{aligned} \quad (6)$$



The kernel function  $K : \Omega \times \Omega \rightarrow \mathbb{R}$  is important to the optimization procedure, since it defines how the underlying vector field is interpolated within a neighborhood of a point, defining the structure of the RKHS. The discrete version of a kernel  $K$  may be represented by the Gram matrix [26], to which we shall also refer as  $K$ , without risk of confusion<sup>1</sup>. Since the computation of this matrix is time-consuming, we shall adopt a recursive implementation of the kernel based on random walks on undirected graphs, easily adaptable to isotropic and anisotropic data. We will also show that it allows us to fit the kernel to the geometry of the structures represented by the volume, even when they are convoluted.

Let  $\Gamma = (G, E, w)$  denote a weighted graph where  $G$  is its set of nodes,  $E \subset G \times G$  is its set of edges, and  $w : G \times G \rightarrow \mathbb{R}_{\geq 0}$  is a weight function. In the rest of this section, each node in  $G$  is associated to a unique voxel in  $I$  ( $|G| = n$ ), and an edge  $e = (u, v) \in E$  connecting  $u \in G$  and  $v \in G$  indicates that the voxels they represent are neighbors. The adjacency between nodes of  $\Gamma$  and their respective edge weights are expressed in matrix form by the  $n \times n$  weighted adjacency matrix  $A(u, v) = w(u, v)$  if  $(u, v) \in E$ ,  $A(u, v) = 0$  otherwise. Also, let  $D = \text{diag}(d(u); u \in G)$  be the diagonal weighted degree matrix of  $\Gamma$ , where  $d(u)$  is the weighted degree of a node  $u \in G$  given by the sum of its weighted adjacent edges  $d(u) = \sum_{v \in G} A(u, v)$ .

A random walk of length  $t$  on a graph  $\Gamma$  is a random process that begins at some starting node  $s_0 \in G$ , and then repeats the following procedure  $t$  times: randomly choose a node  $u$  among the neighbors of the current node  $v$  and move to it. If each node contains a loop with weight equal to the sum of weights of its neighbors, then the random walk is called “lazy”, since it may either choose to stay at its current node or move to another one at each step with equal probability. Hereafter, we shall consider  $\Gamma$  a lazy graph. Random walks induce a probability distribution on the nodes of  $G$  at each time step. Let  $S_t$  denote the position of a random walk at time  $t$ . Let  $p_t(v) = P(S_t = v)$  denote the probability that the random walk reaches node  $v$  after  $t$  steps, and let each element of the  $n$ -dimensional vector  $p_t \in \mathbb{R}^{|G|}$  be associated with a node  $v \in G$  and store the probability  $p_t(v)$ . The initial probability distribution  $p_0$  is typically concentrated at node  $s_0$ , since the walk starts there. Thus,  $p_0(v) = 1$ , if  $v = s_0$ , or  $p_0(v) = 0$  otherwise. The probability  $p_{t+1}(v)$  of reaching any  $v$  at step  $t + 1$  depends on all  $P(S_t = u)$ , for each  $u$  in the neighborhood of  $v$  (including itself), and on the probabilities of reaching  $v$  from any of its neighbors at  $t + 1$ . Thus:

$$p_{t+1}(v) = \sum_{e=(u,v) \in E} \frac{w(u,v)}{d(u)} p_t(u), \forall v \in G. \quad (7)$$

The probability evolution equation  $p_{t+1}$  can be written in matrix form as  $p_{t+1} = AD^{-1}p_t$ , where  $AD^{-1} = W$  defines the probability matrix of the transition between nodes in a lazy random walk on the graph  $\Gamma$ . By recursively iterating (7) from the initial state, we obtain  $p_t = W^t p_0$ . Intuitively, the evolution of this probability distribution can be seen as a diffusion

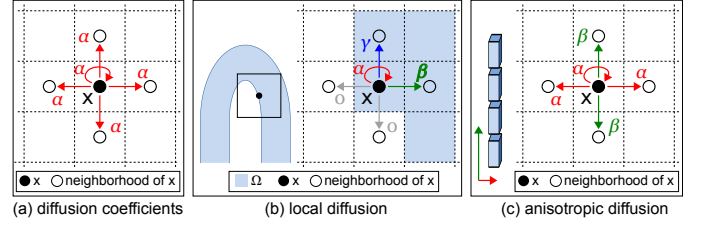


Fig. 4: Computation of diffusion coefficients. In (a) the diffusion is distributed homogeneously among the neighbours. For convoluted shapes, such as pictured in (b), left, the previous model considers points outside the domain  $\Omega$ . To remedy this, (b), right, computes distinct diffusion coefficients over  $\Omega$  only. (c) For anisotropic acquisitions, coefficients vary along the direction of anisotropy.

process where, at each time step, some “substance” running through the graph either remains at the current node, or spreads to a neighbor node according to the diffusion law given by  $p_t = W^t p_0$ . However,  $W$  is not symmetric, which makes computations hard and is an undesirable property for a kernel. Therefore, we take a normalized version  $N$  of  $W$ , such that  $N = D^{-\frac{1}{2}} A D^{-\frac{1}{2}}$ . This matrix is the normalized Laplacian matrix, which is symmetric and semidefinite. It presents the following transition weights:  $n(u, v) = w(u, v) / \sqrt{d(u)d(v)}$ .

From this normalization, we finally define the kernel  $K_t = N^t = (D^{-\frac{1}{2}} A D^{-\frac{1}{2}})^t$ . This matrix respects both properties of an acceptable kernel:  $K_t$  is symmetric since  $A$  is symmetric; and  $K_t$  is positive definite by construction. Note that the size of the kernel will increase as the value of  $t$  increases. We will next illustrate how to use this kernel implementation in practice through a few 2D examples, but the extension to 3D is straightforward by adapting the neighborhood and the weights.

We shall first consider that each point in an image is represented by a graph node, and that each point is connected to itself and to points within its 4-connectivity neighborhood<sup>2</sup>, as shown in Fig. 4a. Also, we will consider each point on the image indifferently, without taking into account the morphology of the object it depicts. This means that, between any two given nodes  $u \in G$ ,  $v \in G$ ,  $n(u, v) = w(u, v)/5$ . However, this transition model is not ideal, especially with respect to high-curvature regions. In these, bands of gray matter with opposite orientation are close, and the inner (or outer) surface of the layer has two nearby sides (Fig. 4b, left). In this case, the kernel does not adapt to the object morphology: if the size of the kernel is higher than the distance separating both sides of the surface, it assigns positive values to pixels located on the opposite side of the ribbon, as well as on the space between both sides. We propose to adapt the kernel locally to the geometry of the volume (Fig. 4b, right) to address such cases. To this purpose, we will consider that a point  $y$ , represented by node  $v \in G$ , is in the neighborhood of a point  $x$ , represented by  $u \in G$ , if it is in  $\Omega$  and if it is in the 4-neighborhood of  $x$ , or if  $x = y$ . Thus, the diffusion is restricted to  $\Omega$ , and the kernel is adapted to its shape. In the remainder of this paper, only this type of kernel will be used.

In the simplest case where the data to be treated is isotropic,

<sup>1</sup>Both the matrix and the function inherit the required properties of symmetry and positive semidefiniteness.

<sup>2</sup>We shall neglect potential border effects by considering that the objects of interest are sufficiently far from image edges.

it suffices to consider  $\Gamma$  an unweighted graph, which corresponds to a weighted graph with weight function  $w(u, v) = 1$ ,  $u \in G, v \in G$ , if  $e = (u, v) \in E$ ; otherwise,  $w(u, v) = 0$ . To deal with anisotropic images, we define edge weights as follows: consider a 2D image with anisotropic factor  $l$  in the vertical axis (i.e., the image resolution is  $X\text{mm} \times lX\text{mm}$ ). In order to obtain a ratio of  $l = \sqrt{\alpha/\beta}$  between the extent of the kernel in the horizontal axis relative to the vertical axis (Fig. 4c), we set the vertical edge weights to  $\beta = 5/(3l^2 + 2)$ , while the horizontal edges and loops are assigned a weight of  $\alpha = (5l^2)/(3l^2 + 2)$ .

#### F. Template estimation for population analyses

Our method allows extraction of a central surface and estimates a local thickness map for an individual subject. They can in turn be used to study patterns of differences in thickness and/or central surface shapes between groups of subjects (e.g., a group of healthy subjects and one with a given disease). Relying on the approach presented by [27] and detailed in Appendix IV, we propose to compare the individual local thickness maps in a common space by 1) building a template surface from all the surfaces associated to such maps and 2) projecting thickness maps onto this template. Briefly, a template and all diffeomorphic deformations from each subject to the template are simultaneously computed using a sparse parametrization. Each individual thickness map is then projected onto the template by back-projecting the vertices of the template surface mesh onto the individual map and interpolating nearby thicknesses using radial basis functions.

### III. EXPERIMENTS AND RESULTS

#### A. Robustness with respect to kernel size and anisotropy

To study the robustness of the approach with respect to anisotropy, we simulated data with increasing anisotropy levels from a segmentation of a quasi-isotropic post-mortem specimen. In addition, we studied the influence of the kernel size on the measurements.

1) *Subjects*: We used a manual segmentation of a 9.4T MR scan acquired for “Subject 1R”, a *post-mortem* specimen made available in the Penn Hippocampus Atlas [10] (<https://www.nitrc.org/projects/pennhippoatlas/>).

2) *MR acquisition*: The above 9.4T MR scan had been acquired at a resolution of  $0.20\text{mm} \times 0.20\text{mm} \times 0.30\text{mm}$  (here the  $z$  direction represents the hippocampus long axis).

3) *Segmentation*: Instead of using the hippocampal sub-region segmentation available for this specimen from the Penn Hippocampus Atlas project, the authors resegmented the hippocampus across its head, body and tail, following the protocol described in Appendix I in order to separate the stratum pyramidale from the SRLM and to guarantee a 3D model of the hippocampus that preserves the convolutions of the structure, especially in the cornu Ammonis (Fig. 2b).

4) *Central surface and thickness estimation*: Applying our method to the segmentation above, we obtained the results depicted in Fig. 5. The original shape of the hippocampal ribbon is correctly encoded by the central surface representation, presenting the same sheet-like topology and preserving the digitations in the hippocampal head of the original volume.

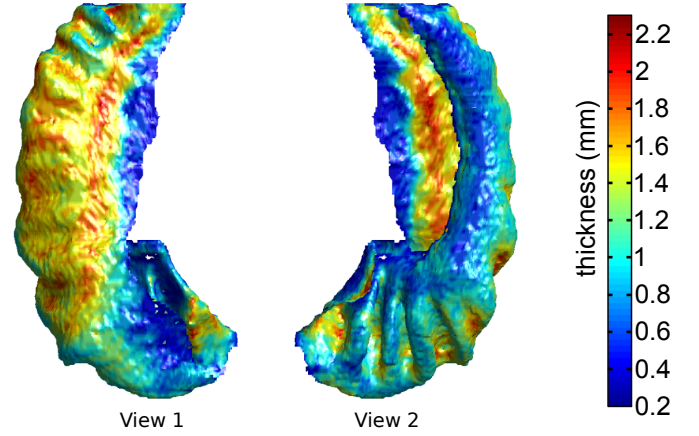


Fig. 5: Thickness map plotted over its associated central surface (shown from two distinct angles) computed from a segmentation of the 9.4T T2-weighted MRI of “Subject 1R” from the Penn Hippocampus Atlas.

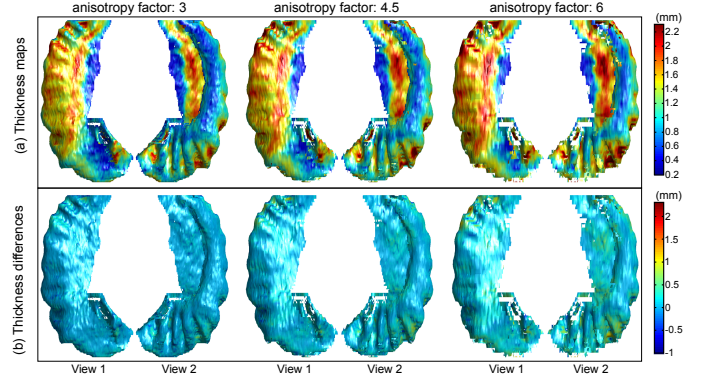


Fig. 6: Influence of anisotropy. (a) Thickness maps (in mm) plotted over their associated central surface for each subsampling factor. (b) Thickness differences (in mm), where positive and negative values indicate over- and under-estimation respectively.

5) *Influence of kernel size*: We computed central surfaces and thickness maps for kernel sizes  $t'$  in  $\{3, 5, 10, 15\}$ . We compared the central surface at reference  $t = 10$  to all remaining  $t'$ , with three metrics: correlations between thickness estimates, mean distances between corresponding points and mean thickness differences. The kernel size was found to have minute influence on the output central surface (Table I).

6) *Influence of anisotropy*: Although there is no actual ground truth of local hippocampal ribbon thickness measures for the post-mortem atlas, we expect its high and quasi-isotropic resolution to provide reasonable thickness estimates. To assess the robustness of our algorithm to anisotropy, we simulated segmentation data with a lower resolution perpendicular to the coronal plane. We subsampled the original segmentation by considering one slice out of  $f$  ( $f \in \{2, 3, 4, 5, 6\}$ ) in the direction of the hippocampal long axis and multiplying the slice thickness by the corresponding subsampling factor (3, 4.5, 6, 7.5 and 9 respectively).

Fig. 6 shows for each subsampling factor in  $\{2, 3, 4\}$  its associated thickness map plotted over the corresponding central surface, as well as thickness differences at each point of the subsampled surface to the closest point on the original

Segment	Thickness Correlation			Mean Abs. Thickness Difference (mm)			Mean Inter-Surface Distance (mm)		
	Kernel size			Kernel size			Kernel size		
	3	5	15	3	5	15	3	5	15
Head	0.98	0.99	0.99	0.040	0.027	0.024	0.02	0.02	0.01
Body	0.99	1.00	1.00	0.024	0.013	0.009	0.02	0.01	0.01
Tail	0.98	0.99	0.99	0.047	0.032	0.025	0.02	0.02	0.01
All	0.99	0.99	1.00	0.037	0.024	0.020	0.02	0.01	0.01

TABLE I: Influence of kernel size. Correlations (Pearson’s  $r$ ) and mean absolute differences between thickness values, as well as mean distances between central surfaces computed from the original volume with a kernel size  $t = 10$  and  $t' \in \{3, 5, 15\}$ .

surface. The resulting central surfaces and thickness maps are very similar. The main spots of thickness differences are the folds of the hippocampal tail. This is likely due to the fact that the folds of the tail are approximately parallel to the coronal plane, which potentially results in inaccurate representation of those folds in the subsampled images where slices are averaged perpendicular to that plane to simulate anisotropy. The orientation of the hippocampal head folds (approximately orthogonal to the coronal plane) and the comparatively lower differences observed for this segment support the previous assertion.

The extent of the differences across all hippocampal segments remains, nevertheless, limited. Furthermore, the robustness of the thickness estimates with respect to anisotropy was quantitatively assessed, using the same measures as for the influence of kernel size. These results are shown in Table II. For subsampling factors in  $\{2, 3, 4, 5\}$ , we found very strong correlations between thickness estimations (between 0.91 and 0.99) and very low mean thickness differences (between 0.04mm and 0.23mm) in the hippocampal body. Slightly stronger differences were found in the head and in the tail, but they remain within a relatively low range of values (at most 0.36mm for the tail and for the highest anisotropy). At an higher subsampling factor 6, corresponding to a slice thickness of 1.8mm, a decrease in performance was noted, with thickness correlations in the body falling to 0.77.

### B. Influence of inter-rater variability

1) *Subjects*: We analyzed the influence of inter-rater variability on a set of 7T MRI from four control subjects. The population was composed of two men and two women, with a mean age of 36 years (range 25-55 years).

2) *MR acquisition*: High-resolution oblique coronal 2D T2-weighted fast spin-echo images were acquired on a Siemens 7T MRI scanner (Erlangen, Germany) using a 32-channel head coil, as per the acquisition protocol described in [9]. Each image corresponds to a volume composed of 1.2mm-thick slices with 0.3mm $\times$ 0.3mm in-plane resolution.

3) *Segmentation*: For each image, two expert raters (authors J. Germain and L. Marrakchi-Kacem) manually segmented hippocampal subregions across the whole hippocampus following the protocol described in Appendix I.

4) *Central surface and thickness estimation*: The central surfaces and thickness maps of each control were extracted across the full length of the hippocampus for each hemisphere and for each rater using a kernel size parameter  $t = 10$ . Fig. 7,

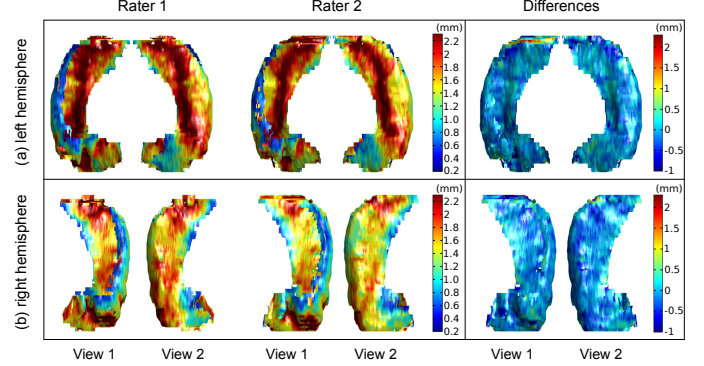


Fig. 7: (a) Left hemisphere: central surfaces and respective local thickness maps obtained from manual segmentations of hippocampal subregions from the 7T MRI of a healthy subject (left). The same data were segmented by expert raters 1 and 2. The inter-rater local thickness differences map are shown on the right. (b) Same illustration for the right hemisphere.

left illustrates the corresponding thickness maps obtained for both experts.

5) *Inter-rater analysis*: Taking each of our 8 control hippocampi, we paired the thickness map for rater 1 with the corresponding map for rater 2. In a similar fashion to Sect. III-A, for each of the pairs we computed the mean absolute thickness differences, the mean inter-surface distances and thickness correlations across the head, body, tail and full length of the hippocampus. We finally averaged the above statistics across the 4 pairs in each hemisphere to produce the results presented in Table III. Mean absolute thickness differences and mean inter-surface distances in the hippocampal head and tail were found to be lower than 0.41mm and 0.29mm respectively, and an even stronger agreement was observed in the hippocampal body, for which correlations between thickness measurements were high (greater than 0.86) whereas the mean absolute thickness difference and the mean inter-surface distance were low (lower than 0.18 and 0.15 respectively). Fig. 7, right shows examples of inter-rater differences for the thickness maps.

### C. Application to *in vivo* 7T MRI group studies

To evaluate how our method can detect differences between populations, it was applied to *in vivo* 7T MRI data (acquired at the Univ. of Minnesota as described in [11]) from nine healthy controls, and eight adult patients suffering from temporal lobe epilepsy (TLE).

1) *Subjects*: All participants provided written consent to participate in this institutional review board-approved study,



Segment	Thickness					Mean Abs. Thickness					Mean Inter-Surface				
	Correlation					Difference (mm)					Distance (mm)				
	Anisotropy					Anisotropy					Anisotropy				
	3	4.5	6	7.5	9	3	4.5	6	7.5	9	3	4.5	6	7.5	9
Head	0.93	0.88	0.80	0.76	0.75	0.10	0.17	0.25	0.35	0.47	0.05	0.07	0.09	0.10	0.10
Body	0.99	0.98	0.96	0.91	0.77	0.04	0.09	0.15	0.23	0.36	0.03	0.04	0.05	0.06	0.07
Tail	0.95	0.89	0.85	0.83	0.79	0.11	0.20	0.29	0.36	0.48	0.05	0.08	0.10	0.13	0.13
All	0.95	0.91	0.86	0.82	0.76	0.09	0.16	0.23	0.32	0.44	0.05	0.06	0.08	0.09	0.10

TABLE II: Influence of anisotropy. Correlations (Pearson's  $r$ ) and mean absolute differences between thickness values, as well as mean distances between central surfaces computed from the original volume and from the subsampled volumes with different anisotropies (3, 4.5, 6, 7.5, 9).

Segment	Left Hemisphere					Right Hemisphere				
	Thickness	Mean	Abs.	Mean	Inter-	Thickness	Mean	Abs.	Mean	Inter-
		Thickness		Surface			Thickness		Surface	
	Correlation	Difference (mm)		Distance (mm)		Correlation	Difference (mm)		Distance (mm)	
Head	0.76	0.24		0.18		0.79	0.25		0.19	
Body	0.90	0.17		0.15		0.86	0.18		0.15	
Tail	0.68	0.41		0.28		0.79	0.28		0.29	
All	0.79	0.24		0.18		0.82	0.23		0.20	

TABLE III: Average correlations (Pearson's  $r$ ) and mean absolute differences between thickness values, as well as mean distances between central surfaces computed from the segmentations of 7T MRI of four subjects by two distinct raters.

which complied with Health Insurance Portability and Accountability Act regulations. Epilepsy subjects and healthy control subjects had never had intracranial surgery, had no contraindication to MRI exposure, had reported no claustrophobia or other reasons for intolerance of MRI scanning, and were not pregnant. Healthy subjects had no neurological, psychiatric or medical condition. The mean age of the 9 healthy subjects was 26 years (range 19-46 years). Four were women. Epilepsy subjects were recruited among clinic patients of one investigator at the University of Minnesota (T. R. Henry). Mean age for the 8 epilepsy subjects was 28 years (range 20-49 years). Five were women. Five patients had left-sided ictal EEG onsets with ipsilateral hippocampal atrophy and T2 hyperintensity, and three had these EEG and hippocampal MRI abnormalities on the right side.

2) *MR acquisition*: High-resolution oblique coronal 2D T2-weighted fast spin-echo images were acquired on a Siemens 7T MRI scanner (Erlangen, Germany), using a 16-channel head coil. Each image corresponds to a volume composed of 1.2mm-thick slices with 0.25mm $\times$ 0.25mm in-plane resolution, obtained through the protocol described in [11].

3) *Segmentation*: Manual segmentations were performed by authors M. Chupin and É. Gerardin. Since manually delineating hippocampal subregions across the full length of the hippocampus is highly labor intensive, the segmentations in this study were restricted to the hippocampal body.

4) *Group study*: To assess differences between each TLE patient group (left ictal onset and right ictal onset) and the controls, we computed four templates. For each hemisphere, one template was estimated from the central surfaces extracted from controls (Controls-R/L) and the ipsilateral side of patients (TLE-IR/IL), and another template was estimated from controls (Controls-R/L) and the contralateral side of patients (TLE-CR/CL). The parameters adopted for template creation were the same in all four experiments.

Fig. 8a shows thickness values averaged across the hip-

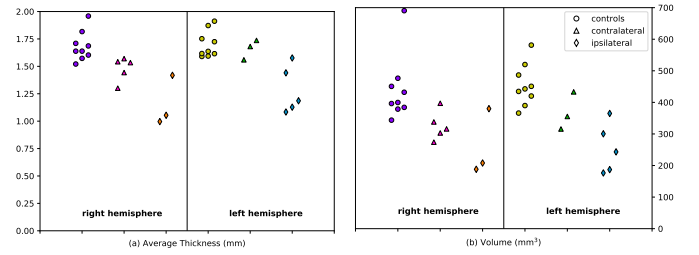


Fig. 8: (a) hippocampal thickness averaged over the body part of the hippocampal ribbon for each studied subject (controls, contralateral and ipsilateral TLE patients). (b): hippocampal ribbon volumes across the body part of the hippocampus.

poampal body of ipsi/contralateral TLE patients and controls. Ipsilaterally, patients had lower thickness values than controls and there was no overlap between the two. Contralaterally, there was also a trend for lower values in the left TLE patients (right hippocampus) compared to controls. As shown in Fig. 8b, similar results were found replacing thickness values with the volumes of the hippocampal ribbon: contralaterally, TLE patients tended to have lower volumes than controls, a tendency which was even stronger ipsilaterally. This agreement between thickness and volume measures was confirmed by Spearman's rank correlation coefficients (computed across all subjects) of 0.84 and 0.83 for the left and right hemisphere respectively. In both hemispheres a clearer separation between the classes was achieved using thickness measures, with a greater variance observed in volumes for each TLE patient groups and controls.

Fig. 9 shows maps of the average thickness values across the full length of the hippocampal body of controls and of the TLE patients as well as their pointwise differences. Supporting the global trend, a strong thinning of the stratum pyramidale can be noted ipsilaterally to the seizure focus. Slightly lower thinning was also found contralaterally, but the

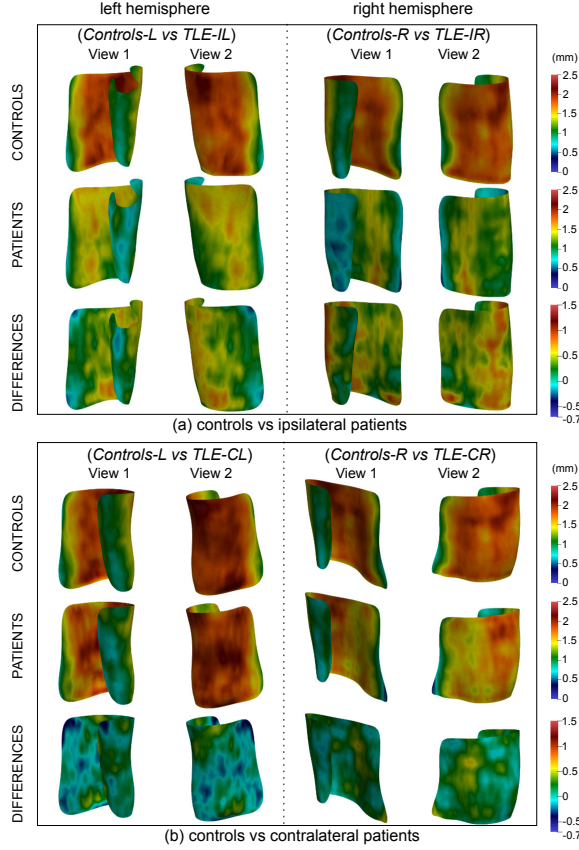


Fig. 9: Average thickness maps computed for experiments (a) “Controls-L vs TLE-IL”+“Controls-R vs TLE-IR” and (b) “Controls-L vs TLE-CL”+“Controls-R vs TLE-CR”. Thickness values (in mm) are given for controls and patients as well as their pointwise differences. As a reference, the hippocampal head should be on the continuation of left of the inferior portion of the surfaces.

thinning pattern was much milder than ipsilaterally. Due to the small number of subjects available for this study, these results should be interpreted as trends and would need to be confirmed in a larger population through statistical tests to assess their significance. Nevertheless, the pattern is consistent with medical knowledge and with previous studies [10], [11], [28].

#### IV. DISCUSSION

We propose a new variational formulation that estimates smooth vector fields through regularization kernels in order to compute a central surface representation and to estimate a local thickness map of the hippocampal ribbon from high-resolution 7T MRI scans. We studied the robustness of our approach with respect to anisotropy and to inter-rater variability. Additionally, we showed how it can detect local alterations in diseased populations.

Our formulation estimates a vector field across the boundaries of the hippocampal ribbon. Thanks to its regularization through a kernel in an RKHS, the field is diffeomorphic, which results in unique and non-crossing streamlines from one boundary to the other. From these properties, it ensues that the measure of thickness and the central surface representation,

both computed from distances integrated along the streamlines, are unique and unambiguous, in contrast with previous approaches that rely on Euclidean distances [14], [21]. Like our method, [22] defines thickness according to streamline lengths. It is worth noticing, however, that our vector field is directly estimated through a unified mathematical framework, rather than through a combined scheme for gradient computation and tangent vector field integration. Besides, we have specifically adjusted our own approach to the nature of hippocampi segmented from high-resolution MRI. As such, our method is suited to partially-defined boundaries, can handle highly anisotropic, as well as isotropic, segmentations, and our kernels have been designed to reflect the convolutions of the ribbon, a prominent feature of the hippocampal head.

We first confirmed the robustness of the algorithm to kernel size variation. We simulated anisotropic segmentations by reducing the number of slices from the segmentation along the anterior-posterior axis. Such “ad hoc” segmentations are likely less accurate and tridimensionally consistent than segmentations from anisotropic acquisitions, resulting in potentially larger anisotropy-induced thickness variations. Despite this, we found overall very small disparities, with the exception of convolutions oriented approximately perpendicular to the coronal plane, implying thus that our method is well suited to anisotropic acquisitions.

The second experiment studied robustness to inter-rater variability of the segmentation. While moderately high correlations were found for the head and the tail of the hippocampus, a good agreement was generally reached in the hippocampal body, suggesting that our thickness measures can be reproduced across different raters. We believe that the higher variability in the head and tail, compared to the body, is mainly linked to the inter-rater variability of the segmentation. Indeed, the inter-rater Dice coefficients (for the segmentations of substructures CA-SP and subiculum, which are used for thickness estimation) are higher in the body than in the head and the tail (see Tables I and II of the Appendix). Head and tail are more difficult to segment, because they have a more convoluted geometry and are more affected by partial volume between consecutive slices. It is also possible that the convolutions of the head and tail have directly influenced the inter-variability of thickness measures, even though our results on inter-rater variability of segmentations support the idea that it mainly comes from the segmentation.

We finally applied the method to study differences between TLE patients and controls from *in vivo* 7T MRI. We found strong atrophies ipsilaterally to the seizure focus in both left and right TLE patients with respect to controls, with no overlap in individual mean thickness values between TLE patients and controls. Such a result could indicate hippocampal sclerosis and agrees with the vast literature showing ipsilateral volume reduction and shape abnormalities in patients with TLE (see [29], [30] for examples). We also observed mean thickness values to be lower for left TLE than for right TLE contralaterally to the focus, as also found by [31] Though our findings would need to be confirmed with a larger sample of subjects, they nonetheless show how our method can be potentially useful to analyze thickness in populations of patients. This would be



particularly beneficial for patients whose electroclinical signs of TLE are not reflected in abnormal hippocampal volumes.

Our study has the following limitations. First, even though our results demonstrate the potential of this approach to detect alterations in diseased populations, this will need to be confirmed in larger samples as well as in patients with other types of pathologies (e.g. Alzheimer's disease). Then, while the approach is not specific to the segmentation or acquisition protocols that were used in our experiments, it will be necessary to study its performance when used in combination with other protocols. Future work will thus need to evaluate our approach with other segmentation protocols as well as with automated segmentation tools. Another limitation is the lack of validation of absolute thickness measurements with respect to a histological ground truth. Such histological slices were unfortunately unavailable to us. This deserves to be addressed in a future work.

## V. CONCLUSION

We proposed a method to measure the local thickness of the hippocampus from high-resolution 7-Tesla MRI. To that purpose, we introduced an original variational formulation that estimates smooth vector fields through regularization kernels. The method provides a central surface representation of the hippocampal ribbon onto which local thickness measures are mapped. We studied the influence of anisotropy and inter-rater variability. We found overall good robustness. Note, however, that robustness was higher in the body, compared to the head and tail which are more difficult to segment. Studying patients with temporal lobe epilepsy showed the potential of the technique to detect local alterations in diseased populations, although this will need to be confirmed in larger samples. Overall, our method allows studying local thickness and shape alterations of hippocampal subregions. With the increasing availability of 7-Tesla MRI, it has the potential to become a useful tool to study alterations in different pathologies which affect the hippocampus, such as Alzheimer's disease, epilepsy or depression. It is made freely available to the community (code: <https://github.com/aramis-lab/hiplay7-thickness>, postmortem segmentation: <https://doi.org/10.5281/zenodo.3533264>).

## REFERENCES

- [1] E. Geuze *et al.*, "MR-based in vivo hippocampal volumetrics: 2. findings in neuropsychiatric disorders," *Molecular psychiatry*, vol. 10, no. 2, p. 160, 2005.
- [2] H. Duvernoy, *The Human Hippocampus: Functional Anatomy, Vascularization and Serial Sections with MRI*. Springer, 2005.
- [3] T. L. Babb *et al.*, "Temporal lobe volumetric cell densities in temporal lobe epilepsy," *Epilepsia*, vol. 25, no. 6, pp. 729–740, Dec 1984.
- [4] B. T. Hyman *et al.*, "Alzheimer's disease: cell-specific pathology isolates the hippocampal formation," *Science*, vol. 225, no. 4667, pp. 1168–1170, Sep 1984.
- [5] L. E. Wisse *et al.*, "A harmonized segmentation protocol for hippocampal and parahippocampal subregions: Why do we need one and what are the key goals?" *Hippocampus*, vol. 27, no. 1, pp. 3–11, 2017.
- [6] J. L. Winterburn *et al.*, "A novel in vivo atlas of human hippocampal subfields using high-resolution 3 T magnetic resonance imaging," *Neuroimage*, vol. 74, pp. 254–265, 2013.
- [7] J. M. Theysohn *et al.*, "The human hippocampus at 7 T in vivo MRI," *Hippocampus*, vol. 19, no. 1, pp. 1–7, Jan 2009.
- [8] L. E. M. Wisse *et al.*, "Subfields of the hippocampal formation at 7 T MRI: in vivo volumetric assessment," *Neuroimage*, vol. 61, no. 4, pp. 1043–1049, Jul 2012.
- [9] L. Marrakchi-Kacem *et al.*, "Robust imaging of hippocampal inner structure at 7T: in vivo acquisition protocol and methodological choices," *Magnetic Resonance Materials in Physics, Biology and Medicine*, vol. 29, no. 3, pp. 475–489, 2016.
- [10] P. A. Yushkevich *et al.*, "A high-resolution computational atlas of the human hippocampus from postmortem magnetic resonance imaging at 9.4 T," *Neuroimage*, vol. 44, no. 2, pp. 385–398, Jan 2009.
- [11] T. R. Henry *et al.*, "Hippocampal sclerosis in temporal lobe epilepsy: findings at 7T," *Radiology*, vol. 261, no. 1, p. 199–209, 2011.
- [12] R. La Joie *et al.*, "Hippocampal subfield volumetry in mild cognitive impairment, Alzheimer's disease and semantic dementia," *Neuroimage Clin*, vol. 3, pp. 155–162, 2013.
- [13] S. G. Mueller *et al.*, "Hippocampal atrophy patterns in mild cognitive impairment and Alzheimer's disease," *Hum Brain Mapp*, vol. 31, no. 9, pp. 1339–1347, Sep 2010.
- [14] B. Fischl and A. M. Dale, "Measuring the thickness of the human cerebral cortex from magnetic resonance images," *Proc Natl Acad Sci U S A*, vol. 97, no. 20, pp. 11 050–11 055, Sep 2000.
- [15] M. J. Clarkson *et al.*, "A comparison of voxel and surface based cortical thickness estimation methods," *Neuroimage*, vol. 57, no. 3, pp. 856–865, 2011.
- [16] G. A. Kerchner *et al.*, "Hippocampal CA1 apical neuropil atrophy in mild alzheimer disease visualized with 7-T MRI," *Neurology*, vol. 75, no. 15, pp. 1381–1387, Oct 2010.
- [17] C. La *et al.*, "Hippocampal CA1 subfield predicts episodic memory impairment in parkinson's disease," *NeuroImage: Clinical*, vol. 23, p. 101824, 2019.
- [18] A. C. Burggren *et al.*, "Reduced cortical thickness in hippocampal subregions among cognitively normal apolipoprotein E  $\epsilon$ 4 carriers," *Neuroimage*, vol. 41, no. 4, pp. 1177–1183, Jul 2008.
- [19] A. D. Ekstrom *et al.*, "Advances in high-resolution imaging and computational unfolding of the human hippocampus," *Neuroimage*, vol. 47, no. 1, pp. 42–49, Aug 2009.
- [20] M. Donix *et al.*, "Longitudinal changes in medial temporal cortical thickness in normal subjects with the APOE-4 polymorphism," *Neuroimage*, vol. 53, no. 1, pp. 37–43, Oct 2010.
- [21] P. A. Yushkevich *et al.*, "Automated volumetry and regional thickness analysis of hippocampal subfields and medial temporal cortical structures in mild cognitive impairment," *Hum Brain Mapp*, vol. 36, no. 1, pp. 258–287, Jan 2015.
- [22] J. DeKraker *et al.*, "Unfolding the hippocampus: An intrinsic coordinate system for subfield segmentations and quantitative mapping," *NeuroImage*, vol. 167, pp. 408–418, 2018.
- [23] M. M. Zeineh *et al.*, "Unfolding the human hippocampus with high resolution structural and functional MRI," *Anat Rec*, vol. 265, no. 2, pp. 111–120, Apr 2001.
- [24] S. E. Jones *et al.*, "Three-dimensional mapping of cortical thickness using Laplace's equation," *Hum Brain Mapp*, vol. 11, no. 1, pp. 12–32, Sep 2000.
- [25] J. M. Phillips and S. Venkatasubramanian, "A gentle introduction to the kernel distance," *CoRR*, vol. abs/1103.1625, 2011.
- [26] T. Hofmann *et al.*, "Kernel methods in machine learning," *Ann. Statist.*, vol. 36, no. 3, pp. 1171–1220, 06 2008.
- [27] S. Durrleman *et al.*, "Morphometry of anatomical shape complexes with dense deformations and sparse parameters," *Neuroimage*, vol. 101, pp. 35–49, Nov 2014.
- [28] J.-C. Schoene-Bake *et al.*, "In vivo mapping of hippocampal subfields in mesial temporal lobe epilepsy: relation to histopathology," *Hum Brain Mapp*, vol. 35, no. 9, pp. 4718–4728, Sep 2014.
- [29] G. D. Cascino *et al.*, "Magnetic resonance imaging-based volume studies in temporal lobe epilepsy: pathological correlations," *Ann Neurol*, vol. 30, no. 1, pp. 31–36, Jul 1991.
- [30] N. Bernasconi *et al.*, "Mesial temporal damage in temporal lobe epilepsy: a volumetric MRI study of the hippocampus, amygdala and parahippocampal region," *Brain*, vol. 126, no. Pt 2, pp. 462–469, Feb 2003.
- [31] S. S. Keller *et al.*, "Concomitant fractional anisotropy and volumetric abnormalities in temporal lobe epilepsy: cross-sectional evidence for progressive neurologic injury," *PLoS One*, vol. 7, no. 10, p. e46791, 2012.

# Supplementary Material: A Diffeomorphic Vector Field Approach to Analyze the Thickness of the Hippocampus from 7T MRI

## I. HIPPOCAMPAL SUBREGIONS MANUAL SEGMENTATION PROTOCOL

This appendix describes the protocol that we devised and used to segment the subregions of the hippocampus. The protocol was first designed on post-mortem T2-weighted images and subsequently adapted in order to handle in-vivo T2-weighted images. It extends the previous protocol presented in [1] and [2] through several aspects: i) boundary definition using post-mortem ultra-high-resolution MRI and subsequent adaptation to in-vivo 7T MRI; ii) reduced number of arbitrary landmarks; iii) segmentation over the full length of the hippocampus and not only the hippocampal body.

In order to design the protocol, we used post-mortem data acquired at 9.4T ( $0.3 \times 0.2 \times 0.2$ mm resolution) by the University of Pennsylvania [3] and used in Section III-A of the present paper as well as in-vivo data acquired at Neurospin (CEA Saclay, France, see [4]) on a 7T Siemens MRI scanner ( $0.3 \times 0.3 \times 1.2$ mm resolution) with a Nova Medical 32 receiving channel coil, perpendicular to the hippocampal main axis.

Anatomical boundaries are defined based on [5] and [6] as well as on in-house histological sections. In both in-vivo and ex-vivo data we identify the uncus (the most medial part of the temporal lobe). Referring to its position, we isolate three subparts of the hippocampus (body, head and tail) for which the following structures (see Fig. 1) are delineated: 1) alveus; 2) SRLM assumed to correspond to the strata radiatum, lacunosum and moleculare of CA1-3 and the strata lacunosum and moleculare of the subiculum (i.e. the layers poorer in neuronal bodies); 3) hilum corresponding to the stratum pyramidale of CA4 and the stratum granulosum and polymorphic layer of DG, which are the layers richer in neuronal bodies; 4) Cornu Ammonis Stratum Pyramidale (CA-SP), assumed to correspond to the stratum pyramidale of CA1-3, the layer richer in neuronal bodies of CA1-3; 5) subiculum-SP corresponding to the stratum pyramidale of the subiculum, layer richer in neuronal bodies of the subiculum; 6) fimbria. The structures are segmented in the coronal plane, slice by slice, following a specific order whenever possible (alveus, SRLM, hilum, CA-SP, subiculum, fimbria), with references to sagittal and axial planes to ensure 3D consistency. Specific definitions are considered for the hippocampal body, head and tail, as the shape of the digitationes hippocampi and the change of orientation in head and tail make segmenting those a much more complex task.

The manual segmentation protocol consists of two steps: the limits of the head, body and tail of the hippocampus are first

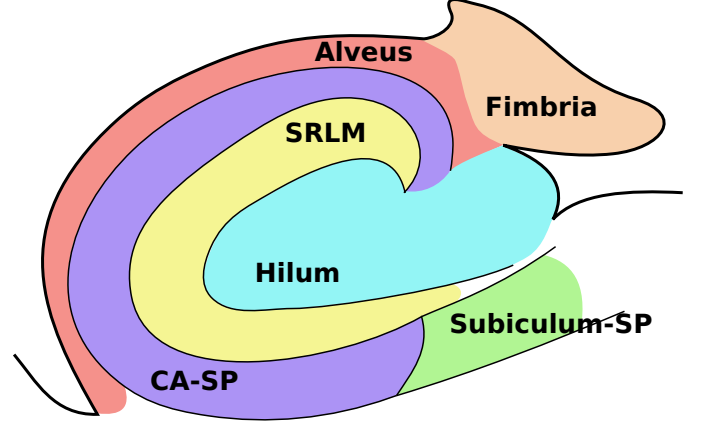


Fig. 1: Map (coronal view, adapted from [5]) of the hippocampal subregions the segmentation protocol delimits: Alveus; SRLM: strata radiatum, lacunosum and moleculare of CA1-3 and strata lacunosum and moleculare of the subiculum; Hilum: stratum pyramidale of CA4 and stratum granulosum plus polymorphic layer of DG; CA-SP: stratum pyramidale of CA1-3; Subiculum-SP: stratum pyramidale of the subiculum; fimbria.

identified, and next the subregions are delineated according to our predefined labels (first in the body, then in the head and finally in the tail).

### A. Head, body and tail identification

The most anterior slice of the hippocampal body is the easiest to delimit: when scrolling from front to back, it corresponds to the first slice where the median part of the hippocampus (the uncus) is no longer visible (Fig. 2a in red). To identify the most posterior slice of the body, we follow a geometric feature: the change in orientation of the main hippocampal axis (Fig. 2b in red), after which the cornu Ammonis and the gyrus dentatus begin to lose their usual C-shaped configuration in coronal planes, whereas the fimbria enlarges and acquires a “fan” shape at the superior-medial border of the hippocampus. Both the most anterior and posterior body limits are confirmed in the sagittal plane.

The most anterior limit of the hippocampus is the beginning of its head, which is easily identifiable. Since the head is anteriorly covered by the alveus, the first head slice is marked by the appearance of gray matter “inside” white matter (Fig. 2c in red).

Finally, the most posterior limit of the hippocampus, the end of its tail, is the hardest to define. It is detected by checking the appearance of a usual sulcus shape. Indeed, in the anterior part of the tail, the cornu Ammonis has a configuration similar

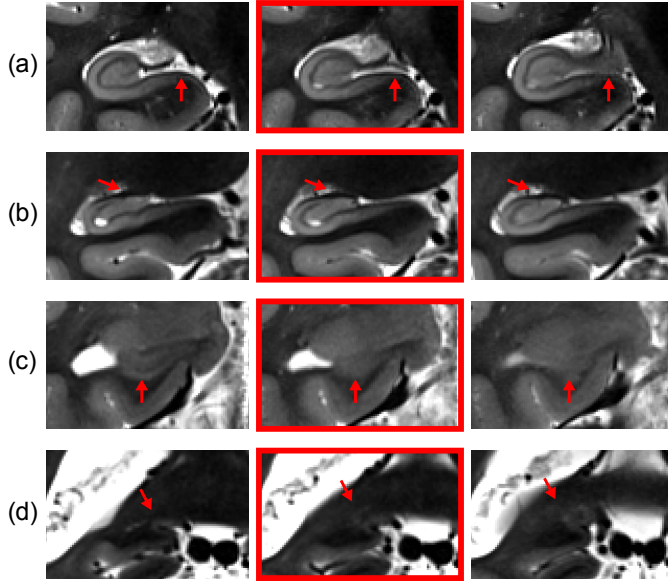


Fig. 2: Identification of: (a) the most anterior slice of the body; (b) the most posterior limit of the body; (c) the anterior limit of the hippocampus; (d) the posterior limit of the hippocampus. The chosen delimiting slices are highlighted in red.

to that of the body. Progressively, the cornu Ammonis presents folds of decreasing size, whereas small protrusions of the gyrus dentatus are still visible. Then, in the posterior part of the tail, the cornu Ammonis becomes smooth and narrow, until it takes the shape of a “classical” gyrus (Fig. 2d in red).

### B. Segmentation of hippocampal subregions

After the anteroposterior limits of the three main segments (head, body and tail) have been identified, the subregions are delineated within each segment separately. First, the hippocampal body is segmented, from the most anterior to the most posterior slice. Next, the head is segmented from the most posterior to the most anterior slice, since it is easier to segment the posterior part of the head by taking into account the delineation of the body. To conclude, we segment the tail from the most anterior to the most posterior slice. At all stages, references are made to sagittal and axial planes to ensure 3D consistency.

1) *Segmentation in the hippocampal body*: Subregions of the hippocampal body, see Fig. 3a, are segmented in the following order.

a) *Alveus*: The inferior border is defined at the junction between the collateral eminence and the alveus when the temporal horn is not collapsed. Its superior border is defined as the point where the alveus enters the hilum.

b) *SRLM*: The SRLM is located between the hippocampal ribbon (CA-SP/Subiculum-SP) and the hilum (when it is present) or as the darker band above the hippocampal ribbon when the hilum is not in front of the ribbon. Its inferior-medial end corresponds to the most medial part of the subiculum, whereas its superior end is clearly visible when CA goes into the hilum. Its other borders are well defined by the signal. In some cases, the vestigial sulcus is dilated and becomes clearly visible; it is not included in the SRLM.

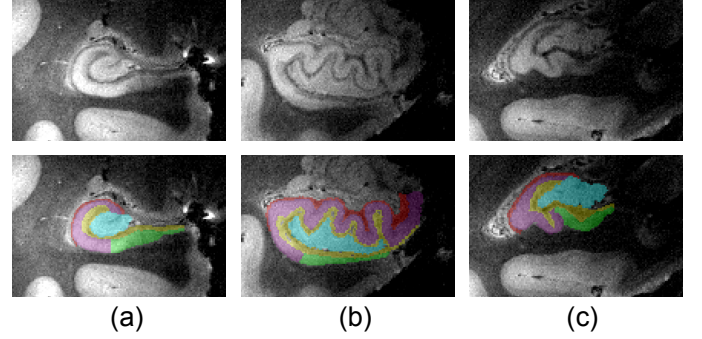


Fig. 3: Top: coronal slices of the hippocampal (a) body, (b) head and (c) tail. Bottom: corresponding manual segmentations. Red - alveus, purple - CA-SP, green - subiculum, yellow - SRLM, light blue - hilum.

c) *Hilum*: Its borders are mostly defined by that of the SRLM, except for its superior and medial limits. The superior limit corresponds to the boundary with CA and does not match a signal contrast. It is therefore defined by tracing an imaginary line between the superior ends of SRLM and alveus. The medial limit with the cerebrospinal fluid (CSF) is defined by a signal change.

d) *CA-SP*: Most of its limits are defined as its boundaries with the alveus, the SRLM and the hilum. The only border that remains to be determined is its inferior boundary with the subiculum. This is defined in a purely geometric manner to correspond to the middle of the hilum so as to mimic the ratio observed in anatomical atlases.

e) *Subiculum*: The lateral border is given by CA-SP, whereas the superior and inferior borders are given respectively by the SRLM and the white matter of the parahippocampal gyrus. The medial limit is arbitrary as there is no clear contrast change between the subiculum and adjacent cortices. It is defined as the inflexion point of the superior part of the parahippocampal gyrus, as it corresponds also to a thinning of the structure.

f) *Fimbria*: It is considered as the round shaped prolongation of the alveus when it separates from CA-SP. Due to image artefacts it is practically impossible to reliably define it on post-mortem data.

2) *Segmentation in the hippocampal head*: See Fig. 3b for an illustration of the segmentation in the hippocampal head. Segmenting the structures relies on an earlier delineation of the uncus and is done in the same order as for the hippocampal body, with the exception of the CA-SP which does not require prior segmentation of the hilum (that is not visible in all slices in the head) and is delineated before it.

a) *Alveus*: The superior border differs from that found in the hippocampal body, for the most anterior slices of the head. In the most anterior slices, the hippocampus is folded on itself and the limit of the alveus is defined as the most medial point of the dark signal band covering the hippocampus. For the other slices, limits are mostly defined as in the hippocampal body.

b) *SRLM*: For the most anterior slices or the most medial parts of posterior slices, the SRLM lies between CA-SP and the subiculum or between separate parts of CA-SP. There, its

position is determined in the sagittal and axial planes to ensure 3D consistency. Outside those areas, it is located between the hippocampal ribbon and the hilum, as in the hippocampal body.

c) *CA-SP*: In the slices where SRLM cannot be clearly delineated, CA-SP is defined as the gray matter below the alveus. In all other slices, SRLM borders with CA-SP. The limit between CA-SP and the subiculum is arbitrarily defined and based on the curvature of SRLM to mimic what is reported in the atlases. In the amygdalo-hippocampal transition area, the superior border with the alveus is geometrically defined. After the posterior part of the uncus separates into its medial part, the segmentation of CA-SP follows the same rules as in the body. When the posterior part of the uncus separates from the ribbon, the subregions within the uncus cannot be easily discriminated and are treated as “uncus” as a whole. In this area, the segmentation of the remainder of CA-SP follows the same rules as in the body.

d) *Hilum*: Its borders with SRLM are defined by a signal change. Due to the complex shape of hippocampal digitations it can embed several connected components in coronal slices.

e) *Subiculum*: The lateral border is defined by CA-SP, whereas the medial border is the same as in the hippocampal body.

3) *Segmentation in the hippocampal tail*: See Fig. 3c for an illustration of the segmentation in the hippocampal tail. Subregions are segmented in approximately the same order as the one followed for the hippocampal body.

a) *Alveus*: The inferior border is defined as in the body. Its superior border is characterized by a thickening of the “fan-shaped” white matter lamina.

b) *SRLM*: It is located between CA-SP and the hilum. Its boundaries follow the same definitions as in the body. The basic frame of the subregions may be identified more easily on sagittal and axial planes, the precise delineation being done in the coronal plane. When no hilum is visible, the same rules as in the anterior part of the head apply.

c) *Hilum*: Its boundaries are defined as a signal change with respect to SRLM. When the body-like organization is no longer visible, the arbitrary limit with CA-SP is defined by the imaginary line between the end of SRLM and the basis of the fan-like white matter superior to the alveus, while ensuring 3D consistency.

d) *CA-SP*: It is defined as the part of the hippocampal ribbon that prolongs CA-SP of the body. Regarding the limits of CA-SP and the subiculum, in the most posterior slices with sulcus-like aspect, only CA-SP is visible. The transition between the body-like aspect and the sulcus-like aspect is to be confirmed on sagittal and axial planes, to ensure 3D consistency.

e) *Subiculum*: It prolongs the part of the subiculum defined in the body and gradually disappears towards the sulcus-like aspect. The medial part follows the same definition as in the body.

### C. Inter-rater variability

Oblique coronal 2D T2-weighted fast spin-echo MR images were acquired on a Siemens 7T MRI scanner (Erlangen,

Germany), using a 32-channel head coil, for a set of 7T MRI of four control subjects (two men and two women, with a mean age of 36 years). Each image corresponds to a volume composed of 1.2mm-thick slices with 0.3mm×0.3mm in-plane resolution. For each image, two expert raters (authors J. Germain and L. Marrakchi-Kacem) manually segmented hippocampal subregions across the whole hippocampus following the protocol described in this appendix.

In order to assess the inter-rater variability of our segmentation protocol, mean inter-rater Dice coefficients averaged across the four subjects were computed (along with their standard deviation) for all subregions of the left and right hippocampi. These are reported in table I and table II respectively.

## II. ELEMENTS OF HILBERT SPACE THEORY

A vector space  $H$  over  $\mathbb{R}$  is a Hilbert space if:  $H$  has a norm induced by an inner product between any two vectors  $h$  and  $h'$  in  $H$ , denoted  $(h, h') \rightarrow \langle h, h' \rangle_H$ , and the associated norm is  $\|h\|_H^2 = \langle h, h \rangle_H$ ;  $H$  is a complete space for the topology associated to the norm. A Hilbert space isometry between two Hilbert spaces  $H$  and  $H'$  is an invertible linear map  $F : H \rightarrow H'$  such that, for all  $h, h' \in H \times H$ ,  $\langle Fh, Fh' \rangle_{H'} = \langle h, h' \rangle_H$ .

If  $H$  only meets the first condition, it is called a pre-Hilbert space, in which the Schwartz inequality holds:  $\forall h, h' \in H \times H$ ,  $\langle h, h' \rangle_H \leq \|h\|_H \|h'\|_H$ .

The dual space of a normed vector space  $H$ , denoted by  $H^*$  is the space containing all continuous linear functionals  $\Phi : H \rightarrow \mathbb{R}$ . We adopt the notation  $\Phi(h) = (\Phi, h)$  for  $\Phi \in H^*$  and  $h \in H$ .  $H$  being a normed space,  $H^*$  also has a normed space structure, defined by:  $\|\Phi\|_{H^*} = \max\{(\Phi, h) : h \in H, \|h\|_H = 1\}$ .

Let  $H$  be a Hilbert space. For all  $h \in H$ , the function  $\Phi_h : h' \rightarrow \langle h, h' \rangle_H$  belongs to  $H^*$ , and by the Schwartz inequality we have  $\|\Phi_h\|_{H^*} = \|h\|_H$ . A Hilbert space  $H$  may be identified with its dual  $H^*$  by the Riesz representation theorem, which states that, if  $\Phi \in H^*$ , there exists a unique  $h \in H$  such that  $\Phi = \Phi_h$ . With a slight abuse of notation, we will identify  $h$  and  $\Phi_h$ .

a) *Reproducing Kernel Hilbert Space (RKHS)*: Intuitively, an RKHS is a Hilbert space that uses a kernel representation to describe a problem in a high-dimensional feature space through continuous linear functionals. Its main properties are listed below. Let  $V$  be a Hilbert space embedded in the space of continuous functions  $C^0(\Omega, \mathbb{R}^d)$ . Consider  $\Omega \subset \mathbb{R}^d$  and take  $x \in \Omega$ . The linear function  $\delta_x$  defined by  $(\delta_x, v) = v(x)$  is called the evaluation function. If  $\delta_x$  is continuous on  $V$ , then  $V$  is called a Reproducing Kernel Hilbert Space (RKHS). For all  $\alpha \in \mathbb{R}^d$ , we will denote by  $\alpha \otimes \delta_x$  the linear form such that  $(\alpha \otimes \delta_x, v) = \alpha^T v(x)$ . By the Riesz theorem, there exists an element  $K_x^\alpha \in V$  such that, for any  $v \in V$ ,  $\langle K_x^\alpha, v \rangle_V = \alpha^T v(x)$ .

The map  $\alpha \Rightarrow K_x^\alpha$  is linear from  $\mathbb{R}^d$  to  $V$ , which implies that, for  $y \in \Omega$ , the map  $\alpha \Rightarrow K_x^\alpha(y)$  is linear from  $\mathbb{R}^d$  to  $\mathbb{R}^d$ . We will denote by  $K(y, x)$  the matrix such that, for  $\alpha \in \mathbb{R}^d$ ,  $x, y \in \Omega$ ,  $K_x \alpha(y) = K(y, x) \alpha$ . This function  $K$  is called the reproducing kernel of  $V$ , and has several interesting properties, such as the self-reproducing property:

Segment	CA-SP	subiculum	SRLM	alveus	hilum	fimbria
Head	0.82(0.01)	0.75(0.02)	0.75(0.03)	0.76(0.03)	0.88(0.02)	N/A
Body	0.86(0.05)	0.87(0.04)	0.82(0.02)	0.79(0.05)	0.92(0.01)	0.72(0.04)
Tail	0.76(0.05)	0.70(0.08)	0.76(0.05)	0.50(0.16)	0.70(0.17)	N/A
All	0.81(0.02)	0.82(0.04)	0.78(0.01)	0.74(0.04)	0.89(0.02)	0.70(0.04)

TABLE I: Left hippocampus: average inter-rater Dice coefficients for manually segmented subregions of the hippocampus. Results are given for the head, body and tail of the hippocampus, as well as for its whole extent, and are presented as *mean(std)*. N/A is indicative of segments where a structure has not been segmented.

Segment	CA-SP	subiculum	SRLM	alveus	hilum	fimbria
Head	0.84(0.02)	0.78(0.04)	0.76(0.01)	0.75(0.03)	0.86(0.05)	N/A
Body	0.87(0.01)	0.88(0.01)	0.83(0.01)	0.74(0.08)	0.92(0.01)	0.72(0.14)
Tail	0.78(0.05)	0.85(0.06)	0.70(0.07)	0.46(0.26)	0.87(0.02)	N/A
All	0.83(0.01)	0.84(0.01)	0.78(0.01)	0.73(0.05)	0.89(0.02)	0.72(0.14)

TABLE II: Right hippocampus: average inter-rater Dice coefficients for manually segmented subregions of the hippocampus. Results are given for the head, body and tail of the hippocampus, as well as for its whole extent, and are presented as *mean(std)*. N/A is indicative of segments where a structure has not been segmented.

$\forall x, y \in \Omega, \alpha, \beta \in \mathbb{R}^d, \langle K(\cdot, x)\alpha, K(\cdot, y)\beta \rangle_V = \alpha_T K_y \beta(x) = \alpha_T K(x, y)\beta$ . By the symmetric property of the inner product, we obtain :  $K(y, x) = K(x, y)^T$ .  $K$  is also positive definite, in the sense that, for any family  $x_1, \dots, x_d \in \Omega$  and any  $\alpha_1, \dots, \alpha_d$ :

$$\sum_{i,j=1}^d \alpha_i \alpha_j K(x_i, x_j) \geq 0 \quad \sum_{i,j=1}^d \alpha_i \alpha_j K(x_i, x_j) = 0 \quad (1)$$

$$\Leftrightarrow \alpha_1 = \dots = \alpha_d = 0$$

Finally, for any  $v \in V^*$ , we have  $\|v\|_{V^*}^2 = \int_{\Omega} v(x)^T K(x, y) v(y) dx dy$ .

### III. PROOFS OF RESULTS

A summary of the mathematical formulation presented in Section II of the present paper is given below, as well as the proofs to theorems enunciated in the same section.

1) *Isotropic images*: Let  $\Omega \subset \mathbb{R}^d$  ( $d = 2$  or  $d = 3$ ) be a domain representing a hippocampal ribbon,  $\partial\Omega$  its boundary, and  $n$  the outward normal to  $\partial\Omega$ . The boundary  $\partial\Omega$  is further decomposed into its inner ( $\partial\Omega_i$ ), outer ( $\partial\Omega_o$ ) and “wall” ( $\partial\Omega_w$ ) parts, such that  $\partial\Omega = \partial\Omega_i \cup \partial\Omega_o \cup \partial\Omega_w$ . Let  $v$  be a smooth vector field  $v$  running from  $\partial\Omega_i$  to  $\partial\Omega_o$ . Consider  $x \in \partial\Omega$  and let  $\epsilon : \partial\Omega \rightarrow \{-1; 0, 1\}$  be a function defining the orientation of the normal vector in  $\partial\Omega$  such that:

$$\epsilon(x) = \begin{cases} -1 & , \text{ if } x \in \partial\Omega_i \quad (\text{inward orientation}) \\ 0 & , \text{ if } x \in \partial\Omega_w \\ 1 & , \text{ if } x \in \partial\Omega_o \quad (\text{outward orientation}) \end{cases}$$

From the theory of reproducing kernel Hilbert spaces (RKHS), a vector space  $V$  is characterized by the choice of a kernel  $K : \mathbb{R}^d \times \mathbb{R}^d \rightarrow \mathbb{R}$ , such that, for any  $(v, x, \alpha) \in V \times \mathbb{R}^d \times \mathbb{R}^d$ , we have:

$$\langle v(x), \alpha \rangle_{\mathbb{R}^d} = \langle v, K(\cdot, x)\alpha \rangle_V. \quad (2)$$

We estimate the vector field  $v$  by maximizing the following functional:

$$J(u, v) = \int_{\partial\Omega} \langle v, \epsilon n \rangle d\sigma + \int_{\Omega} \langle v, u \rangle dx - \frac{1}{2} \|v\|_V^2 \quad (3)$$

where  $u$  is a unit vector field on  $\Omega$  and  $\|\cdot\|_V$  is the Hilbert norm of  $v \in V$ , which is an RKHS.

If both  $u$  and  $\epsilon$  are fixed, the problem is quadratic and  $v$  can be easily calculated from the formula:

$$v(x) = \int_{\partial\Omega} K(x, y) \epsilon(y) n(y) d\sigma(y) + \int_{\Omega} K(x, y) u(y) dy \quad (4)$$

**Proof** For any variation  $\delta v$ , we have:

$$\frac{\partial J}{\partial v} \cdot \delta v = \int_{\partial\Omega} \langle \delta v, \epsilon n \rangle + \int_{\Omega} \langle \delta v, u \rangle - \langle v, \delta v \rangle_V = 0 \quad (5)$$

By choosing  $\delta v = K(\cdot, x)\alpha$  and using the property expressed by (2) in the last term of (5), we have:

$$\langle v(x), \alpha \rangle = \int_{\partial\Omega} \langle K(\cdot, x)\alpha, \epsilon n \rangle + \int_{\Omega} \langle K(\cdot, x)\alpha, u \rangle \quad (6)$$

By applying the relation in (4) to the functional, we have:

$$\begin{aligned} J(u, v) &= \frac{1}{2} \int_{\Omega} u(y)^T K(x, y) u(x) dx dy \\ &+ \int_{\partial\Omega} \epsilon(y)^T n(y) K(x, y) \epsilon(x) n(x) d\sigma(x) d\sigma(y) \quad (7) \\ &= \frac{1}{2} \|u + \epsilon n\|_V^* \end{aligned}$$

Thus, the variational formulation leads to a problem involving the maximization of a dual norm on vector fields. The smoothness of  $v$  is related to the fact that the linear form  $u + \epsilon n$  has a large dual norm.

2) *Extension to anisotropic images*: Let  $\Phi$  be an application that maps a volume  $\Omega$  in physical space to a volume  $\tilde{\Omega} = \Phi(\Omega)$  in the image space. In our case,  $\Phi$  is a linear transformation of type  $\Phi(x, y, z) = (x, y, z/a)$  where  $a$  is the anisotropy factor. We define  $\Psi = \Phi^{-1}$ , and we denote by  $A$  the matrix of the application  $D\Phi$ , and by  $\tilde{n}$  the normal at  $\partial\tilde{\Omega}$ . Also, let  $K_p$  be the kernel in physical space and  $K_i$  the kernel in image space, such that  $K_i(x, y) = K_p(\Phi(x), \Phi(y))$ , and  $V_p$  and  $V_i$ , be, respectively, the RKHS of  $K_p$  and  $K_i$ .



The vector field  $\tilde{v}$  in the image space is given by:

$$\begin{aligned}\tilde{v}(x) &= \int_{\tilde{\Omega}} K_i(x, y) \frac{u(y)}{\det(A)} dy \\ &+ \int_{\partial\tilde{\Omega}} K_i(x, y) \tilde{\epsilon}(y) \frac{A^T \tilde{n}(y)}{\det(A)} d\tilde{\sigma}(y)\end{aligned}\quad (8)$$

**Proof**  $\forall v \in V_p$ , we have  $v \circ \Psi \in V_i$  and  $\|v\|_{V_p} = \|v \circ \Psi\|_{V_i}$ . By substitution in the standard variational formulation (3), we have:

$$\begin{aligned}J(u, v) &= \int_{\partial\Omega} \langle v, \epsilon n \rangle d\sigma + \int_{\Omega} \langle v, u \rangle dx - \frac{1}{2} \|v\|_V^2 \\ &= \int_{\partial\tilde{\Omega}} \langle v \circ \psi, \epsilon n \circ \psi \rangle \det(D\Psi) d\tilde{\sigma} \\ &+ \int_{\tilde{\Omega}} \langle v \circ \Psi, u \circ \Psi \rangle \det(D\Psi) dx - \frac{1}{2} \|v \circ \Psi\|_{V_i}^2\end{aligned}\quad (9)$$

Considering that  $\partial\Omega$  is defined implicitly as the zero level set of a function  $F$ , then, at a point  $x \in \partial\Omega$ , the normal  $n(x)$  is given by  $n(x) = \nabla F(x)$ . The surface  $\partial\tilde{\Omega}$  and the normal  $\tilde{n}(\tilde{x})$  at any point  $\tilde{x} = \Phi(x) \in \partial\tilde{\Omega}$  are given by  $F \circ \Psi$  and  $\nabla(F \circ \Psi)(\tilde{x}) = D\Psi(y)^T n(x)$  respectively.

If we set  $\tilde{v} = v \circ \Psi$  and  $\tilde{u} = u \circ \Psi$ , the first and second terms of (9) become:

$$\int_{\partial\tilde{\Omega}} \frac{\langle \tilde{v}, A^T \tilde{\epsilon} \tilde{n} \rangle}{\det(A)} d\tilde{\sigma} \text{ and } \int_{\tilde{\Omega}} \frac{\langle \tilde{v}, \tilde{u} \rangle}{\det(A)} dx.$$

Similarly to (5) in the isotropic case, we can write the following variational formulation:

$$\frac{\partial J}{\partial v} \cdot \delta \tilde{v} = \int_{\partial\tilde{\Omega}} \frac{\langle \delta \tilde{v}, A^T \tilde{\epsilon} \tilde{n} \rangle}{\det(A)} + \int_{\tilde{\Omega}} \frac{\langle \delta \tilde{v}, \tilde{u} \rangle}{\det(A)} - \langle \tilde{v}, \delta \tilde{v} \rangle_{V_i} = 0 \quad (10)$$

Which, for  $\delta \tilde{v} = K_i(\cdot, x) \alpha$  leads us to

$$\langle \tilde{v}(x), \alpha \rangle = \int_{\partial\tilde{\Omega}} \frac{\langle K_i(\cdot, x) \alpha, A^T \tilde{\epsilon} \tilde{n} \rangle}{\det(A)} + \int_{\tilde{\Omega}} \frac{\langle K_i(\cdot, x) \alpha, \tilde{u} \rangle}{\det(A)} \quad (11)$$

From this, (8) is deduced.

#### IV. TEMPLATE ESTIMATION FOR POPULATION ANALYSES

The approaches followed throughout this article to 1) estimate a template from a set of several thickness maps and 2) project those maps onto the template are presented below.

##### A. Template estimation

We propose to estimate a template central surface based on the approach presented by [7], which is implemented in the freely available software bundle Deformetrica<sup>1</sup>. Although various alternative template creation methods exist [8], [9], [10], [11], a thorough review would be out of the scope of this paper. Here, we shall limit ourselves to a brief description of the approach and to justifying its suitability to our problem.

In brief, the approach proceeds as follows. Given a set of  $N$  subjects and their respective central surfaces  $S^1, \dots, S^N$ , as well as an initial template shape  $T_0$ , the method simultaneously estimates a template shape  $T$  and 3D nonlinear diffeomorphic

deformations that map this template to each  $S^i$ . All shapes are considered to be embedded in 3D space (ambient space), and each template-to-subject deformation is seen as a particular deformation of the underlying 3D space. Template-to-subject deformations are computed with a sparse parametrization [12] of the Large Deformation Diffeomorphic Metric Mapping (LDDMM) framework [13], [14]. For this, the deformation  $\phi^{\alpha_0^i}(T_0)$  from the template to the  $i$ -th subject is parametrized by a set of control points  $c_0$  in the ambient space and their set of associated momentum vectors  $\alpha_0^i$ . Template estimation then translates into the following optimization criterion:

$$\begin{aligned}E(T_0, c_0, \alpha_0^i) &= \sum_{i=1}^N \frac{1}{2\sigma^2} d_W \left( \phi^{\alpha_0^i}(T_0), S^i \right)^2 \\ &+ \sum_{i=1}^N \|v_0^i\|_V^2\end{aligned}\quad (12)$$

where  $\sigma$  can be interpreted as a Lagrange multiplier and  $\|v_0^i\|_V$  is the norm of the initial velocity field  $v_0^i$  in a pre-Hilbert space  $V$ . This norm represents the length of the geodesic path defined by the diffeomorphic flow of  $T_0$  to  $S^i$ . The term  $d_W \left( \phi^{\alpha_0^i}(T_0), S^i \right)^2 = \|\phi^{\alpha_0^i}(T_0), S^i\|_W^2$  is the varifold distance [15] between two shapes, which defines the data attachment term.

Thus, this deformation model provides diffeomorphic (smooth and invertible) deformations which are thought to be consistent with plausible anatomical deformations. This is particularly appealing in order to realistically transport hippocampal subregions across subjects. The parameters  $c_0$  and  $\alpha_0^i$  define a flow of diffeomorphisms that transform the template into subject  $i$ . They are estimated through the minimization of the varifold distance between the deformed template and each  $S^i$ . The varifold metric between surfaces presents various advantages. First, like the currents metric [16], it is robust to inconsistencies in the orientation of mesh normals, as well as to mesh imperfections such as holes or spikes, and it does not require to explicitly mark corresponding landmarks. On the other hand, it can deal with folded shapes better than currents [16]. This latter property is specifically attractive since the hippocampal ribbon presents a highly convoluted surface.

##### B. Projection of thickness maps onto the template

Based on the previous template estimation, the shape variations of the central surfaces can directly be studied through statistical analysis of the deformations that map the template to each individual. However, it would also be desirable to analyze the local thicknesses. This requires the projection of individual thickness maps onto the template central surface.

Consider the central surface as a triangle mesh, composed of a set of faces and vertices, represented by their spatial coordinates in  $\mathbb{R}^d$ , as well as a thickness attribute associated to each vertex. Let  $V_i$  and  $T_i(v_i)$  represent the set of vertices and vertex thickness values of the  $i$ -th central surface mesh. Similarly, let  $V_t$  and  $T_t(v_t)$  be the analogous elements of the template central surface mesh, whereas  $V_t^i$  and  $T_t^i(v_{t^i})$

<sup>1</sup><http://www.deformetrica.org>

represent the same elements for the template central surface mesh transformed according to the registration that maps the template to the  $i$ -th subject. Thickness values for  $v_{ti} \in V_{ti}$  are computed based on those associated to  $v_i \in V_i$  through radial basis function (RBF) interpolation. Among distinct existing RBF functions [17], the one adopted here was introduced by [18] and offers compact support, which ensures locality of the interpolation. This function is defined as:

$$\psi^s(r) = \left(1 - \frac{r}{s}\right)^4 + \left(4\frac{r}{s} + 1\right), \quad (13)$$

where  $r = \|v_{ti} - v_i\|$ ,  $s$  is a scale parameter and  $\psi^s$  is  $C^2$  on  $\mathbb{R}$ .

## REFERENCES

- [1] T. R. Henry *et al.*, “Hippocampal sclerosis in temporal lobe epilepsy: findings at 7T,” *Radiology*, vol. 261, no. 1, p. 199–209, 2011.
- [2] C. Boutet *et al.*, “Detection of volume loss in hippocampal layers in Alzheimer’s disease using 7T MRI: a feasibility study,” *Neuroimage Clin*, vol. 5, pp. 341–348, 2014.
- [3] P. A. Yushkevich *et al.*, “A high-resolution computational atlas of the human hippocampus from postmortem magnetic resonance imaging at 9.4 T,” *Neuroimage*, vol. 44, no. 2, pp. 385–398, Jan 2009.
- [4] L. Marrakchi-Kacem *et al.*, “Robust imaging of hippocampal inner structure at 7T: in vivo acquisition protocol and methodological choices,” *Magnetic Resonance Materials in Physics, Biology and Medicine*, vol. 29, no. 3, pp. 475–489, 2016.
- [5] H. Duvernoy, *The Human Hippocampus: Functional Anatomy, Vascularization and Serial Sections with MRI*. Springer, 2005.
- [6] R. Insausti and D. G. Amaral, “Hippocampal formation,” in *The Human Nervous System: Second Edition*. Elsevier Inc., 2003.
- [7] S. Durrleman *et al.*, “Morphometry of anatomical shape complexes with dense deformations and sparse parameters,” *Neuroimage*, vol. 101, pp. 35–49, Nov 2014.
- [8] S. Joshi *et al.*, “Unbiased diffeomorphic atlas construction for computational anatomy,” *NeuroImage*, vol. 23 Suppl 1, pp. S151–S160, 2004.
- [9] P. T. Fletcher *et al.*, “The geometric median on riemannian manifolds with application to robust atlas estimation,” *Neuroimage*, vol. 45, no. 1 Suppl, pp. S143–S152, Mar 2009.
- [10] T. Chen *et al.*, “Construction of a neuroanatomical shape complex atlas from 3D MRI brain structures,” *Neuroimage*, vol. 60, no. 3, pp. 1778–1787, Apr 2012.
- [11] S. Zhang *et al.*, “3D anatomical shape atlas construction using mesh quality preserved deformable models,” *Computer Vision and Image Understanding*, vol. 117, no. 9, pp. 1061 – 1071, 2013.
- [12] S. Durrleman *et al.*, “Sparse adaptive parameterization of variability in image ensembles,” *Int J Comp Vision*, vol. 101, no. 1, pp. 161–183, 2013.
- [13] S. Joshi and M. Miller, “Landmark matching via large deformation diffeomorphisms,” *Image Processing, IEEE Transactions on*, vol. 9, no. 8, pp. 1357–1370, Aug 2000.
- [14] M. F. Beg *et al.*, “Computing large deformation metric mappings via geodesic flows of diffeomorphisms,” *International Journal of Computer Vision*, vol. 61, no. 2, pp. 139–157, 2005.
- [15] N. Charon and A. Trounev, “The varifold representation of nonoriented shapes for diffeomorphic registration,” *siam J. Imaging Sciences*, vol. 6, no. 4, pp. 2547–2580, 2013.
- [16] M. Vaillant and J. Glaunès, “Surface matching via currents,” *Inf Process Med Imaging*, vol. 19, pp. 381–392, 2005.
- [17] M. D. Buhmann, *Radial Basis Functions*. New York, NY, USA: Cambridge University Press, 2003.
- [18] H. Wendland, “Piecewise polynomial, positive definite and compactly supported radial functions of minimal degree,” *Advances in Computational Mathematics*, vol. 4, no. 1, pp. 389–396, 1995.